Journal of Crystal Growth 419 (2015) 143–148

Contents lists available at ScienceDirect

Journal of Crystal Growth

journal homepage: www.elsevier.com/locate/jcrysgro

Bulk crystal growth, and high-resolution x-ray diffraction results of LiZnP semiconductor material

Benjamin W. Montag [a,*], Michael A. Reichenberger [a], Madhana Sunder [b], Philip B. Ugorowski [a], Kyle A. Nelson [a], Douglas S. McGregor [a]

[a] Semiconductor Materials and Radiological Technologies (S.M.A.R.T) Laboratory, Kansas State University, Manhattan, KS 66506, USA
[b] Bruker AXS Inc, 5465 E. Cheryl Parkway, Madison, WI 53711, USA

ARTICLE INFO

Article history:
Received 1 October 2014
Received in revised form
20 February 2015
Accepted 1 March 2015
Communicated by: A. Burger
Available online 9 March 2015

Keywords:
A1. Radiation
A1. x-ray diffraction
A1. Crystal Structure
A2. Bridgman technique
B1. Lithium compounds
B2. Semiconducting ternary compounds

ABSTRACT

Nowotny–Juza compounds continue to be explored as a candidate for solid-state neutron detectors. Such a device would have greater efficiency, in a compact form, than present day gas-filled ^{3}He and $^{10}BF_3$ detectors. The $^{6}Li(n,t)^{4}He$ reaction yields a total *Q*-value of 4.78 MeV, larger than ^{10}B, an energy easily identified above background radiations. Hence, devices fabricated from semiconducting compounds containing either natural Li (nominally 7.5% ^{6}Li) or enriched ^{6}Li (usually 95% ^{6}Li) may provide a semiconductor material for compact high efficiency neutron detectors. Starting material was synthesized by preparing equimolar portions of Li, Zn, and P sealed under vacuum (10^{-6} Torr) in quartz ampoules lined with boron nitride and subsequently reacted in a compounding furnace [1]. The synthesized material showed signs of high impurity levels from material and electrical property characterizations. A static vacuum sublimation in quartz was performed to help purify the synthesized material [2]. Bulk crystalline samples were grown from the purified material. An ingot 9.6 mm in diameter and 4.0 mm in length was harvested. Individual samples were characterized for crystallinity on a Bruker AXS Inc. D2 CRYSO, energy dispersive x-ray diffractometer, and a Bruker AXS D8 DISCOVER, high-resolution x-ray diffractometer with a 0.004° beam divergence. The (220) orientation was characterized as the main orientation with the D2 CRYSO, and confirmed with the D8 DISCOVER. An out-of-plane high-resolution rocking curve yielded a 0.417° full width at half maximum (FWHM) for the (220) LiZnP. In-plane ordering was confirmed by observation of the (311) orientation, where a rocking curve was collected with a FWHM of 0.294°.

1. Introduction

Nowotny–Juza compounds were originally, and are still today, studied for photonic applications [3–5]. The filled tetrahedral compound class $A^{I}B^{II}C^{V}$ materials consist of the III-V-like compounds with lithium interstitials. These materials are desirable for their zincblende cubic crystal structure, and unlike thin-film and doped devices, the concentration of Li atoms is equal to other constituent atoms, as seen in Fig. 1. The zincblende crystal structure is arranged where the group II atom is located at $\tau_1=(0, 0, 0)a$ where a is the lattice constant, and the group V atom is located at $\tau_2=(1/4, 1/4, 1/4)a$. The spacious cubic structure allows for lithium atoms to fill the interstitial site at $\tau_3=(1/2, 1/2, 1/2)a$ as shown in Fig. 1 [6,7]. The filling of these interstitial sites allows for a lithium-loaded semiconducting material. A variety of the ternary compounds have been synthesized in the past, commonly in graphite lined quartz ampoules [8]. Synthesis in a tantalum lined crucible has also been reported [6]. However, bulk growth of these materials has not been reported. The existing material and electrical properties have been reported from samples procured by direct reaction of elemental and/or binary materials. These samples are generally tiny facets extracted from the reaction mixture, and are usually small and extremely difficult to handle and process into devices

Materials containing ^{6}Li, ^{10}B, ^{113}Cd, ^{157}Gd and ^{199}Hg have been considered for solid-state neutron detectors [9–20]. The $^{10}B(n,\alpha)^{7}Li$ reaction is desirable for the ^{10}B microscopic thermal neutron absorption cross section of 3839 b, but boron-based compounds, such as BP, BN, and BAs have shown limited success, and thus far do not appear promising due to crystal growth and materials preparation problems [17–20]. Thin-film boron devices suffer due to their geometry, where only one reaction product can be absorbed in semiconducting material, therefore producing some signals that can be difficult to distinguish from background and gamma-ray induced events [21]. In addition, because of the reaction product self-absorption, the reactive film thickness is

* Corresponding author. Tel.: +1 785 532 6480; fax: +1 785 532 7057.
E-mail address: bmontag@ksu.edu (B.W. Montag).

http://dx.doi.org/10.1016/j.jcrysgro.2015.03.001
0022-0248/

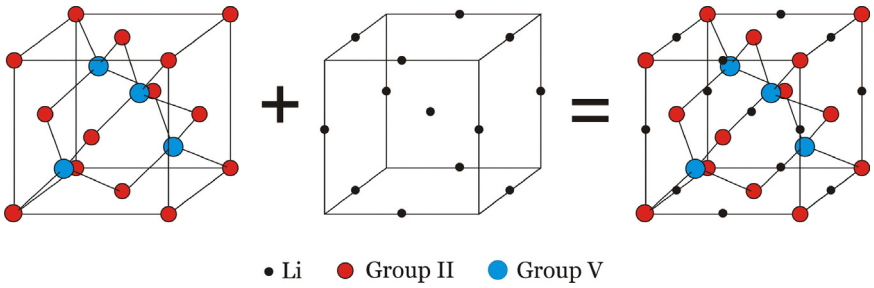

Fig. 1. The cubic crystal structure of $A^{I}B^{II}C^{V}$ compounds.

restricted, and therefore thermal neutron absorption is limited, consequently resulting in a maximum intrinsic detection efficiency of approximately 4.5% [21]. Solid-state detectors containing ^{113}Cd and ^{199}Hg devices also have limited detection efficiency due to the low absorption probability of the prompt gamma-rays that result from ^{113}Cd$(n,\gamma)^{114}$Cd and ^{199}Hg$(n,\gamma)^{200}$Hg reactions [9–12]. The reaction ^{157}Gd$(n,\gamma)^{158}$Gd is desirable for the large ^{157}Gd thermal neutron capture cross section of 240,000 b. Unfortunately, the ^{157}Gd$(n,\gamma)^{158}$Gd reaction yields a spectrum of low energy prompt gamma rays and low energy conversion electrons, all of which are difficult to discern from background radiations [21]. Finally, ^{6}Li has not been explored to the same extent as other thermal neutron absorbers, and has an intrinsic thermal neutron absorption cross section of 940 b. The reaction produces a total Q-value of 4.78 MeV, described by the following reaction,

$$^{6}Li + {}^{1}_{0}n \rightarrow {}^{3}H(2.73\ MeV) + \alpha(2.05\ MeV). \quad (1)$$

LiZnP has been reported to have a bandgap of 2.1 eV, ideal for a room-temperature semiconductor device [8]. A Hall mobility of 1–10 cm^2/V s was reported by Kuriyama [6]. These known electrical properties make LiZnP and other compounds in the class desirable for compact, high neutron sensitivity, solid-state detectors. Synthesis of Nowotny–Juza materials is not trivial. Lithium is very reactive, and the high-pressures that are developed due to the exothermic reactions that occur during the reaction process often result in containment failure. It was found that making the alloy, Li–Zn, prior to reaction aided the reaction process, and resulted in a much higher ampoule yield [1].In addition, melting temperatures of this class of materials have not been completely characterized [6,8,22]. Reported melting temperatures were not consistent with what was observed in the following study. Unfortunately, the difficulties in the synthesis and handling process limit the available physical and electrical property data [3–8,22,23].

2. Experimental details

Described in the following work is a method developed for the bulk crystal growth process of LiZnP, post processing methods, and the high-resolution XRD characterization.

2.1. Bulk crystal growth

LiZnP was synthesized, as described elsewhere, in small batches up to 2.0 g [1]. The synthesized material was purified by a static sublimation process. The process appears to successfully separate the ternary LiZnP material from elemental and binary residual materials that often result from the synthesis process [2]. This purified LiZnP material was subsequently grown into bulk crystals under a high-temperature vertical Bridgman technique.

A 0.5 in. diameter tantalum tube (0.02 in. wall thickness) was cut into a 2.9375 in. long sample containment tube. Tantalum caps were punched, and formed from 0.02 in. thick tantalum sheet. A pyrolytic graphite crucible was custom designed to fit comfortably in the tantalum tube (supplied by Mersen, Inc.). Each of the components were cleaned of oils and contaminants by ultrasonic vibration in a series of solvents namely, isopropanol, acetone and trichloroethylene. The components were loaded into an argon glove box, with minimal oxygen and moisture contamination of less than 0.1%. The bottom cap was welded on the tantalum tube by a Maxstar 150 STL arc welder. The welding torch/stick was fed through the glove box, and the argon environment allowed for the arc plasma to form, and therefore allowed for welding within the box. Purified LiZnP material (1.19 g) was produced, as detailed elsewhere [1,2] was loaded into the pyrolytic graphite crucible, which was loaded into the tantalum vessel. A tantalum cap was welded to the top of the vessel, thereby, making an air-tight containment of LiZnP material and atmospheric pressure argon as shown in Fig. 2.

A bulk crystal was grown in the tantalum vessel contained in a vacuum chamber, equipped with an Omega iR2C series fiber optic thermometer mounted on a two axis rotation stage for alignment purposes. The vacuum chamber was equipped with two feed-throughs connected to an R.D. Mathis LV 400 high-current and low-voltage power source. The tantalum vessel was connected between two electrical connecting oxygen-free plates, referred to as a *copper harness*, depicted in Fig. 3. The copper harness connected to the electrical feed-throughs within a vacuum chamber and these feed-throughs connected to the high-current and low-voltage power source. Continuity was tested to confirm a stable connection outside of the vacuum chamber. The chamber was evacuated, and then purged with ultra-high purity argon at least six times. After the final purge, the chamber pressure was maintained between 300–400 mTorr argon pressure. The current was ramped typically from 0 A to approximately 295–315 A over the course of at least an hour, until the optical thermometer measured approximately 1345 °C at the tantalum surface. Temperature was maintained for at least an hour. The system was then ramped down to room temperature over the following 40 h. The vessel was extracted from the chamber, and opened with a pipe cutter under a pure argon environment. The ingot was harvested, and individual samples were cut from the ingot with a Laser Technology West Ltd. CS400 diamond wire saw while under a constant flow of mineral oil for protection from moisture in the air.

2.2. x-ray diffraction measurements

A LiZnP sample was sliced to $4.077 \times 3.518 \times 2.020$ mm^3, and XRD analysis was performed on one side of the 4.077×3.518 mm^2 face. The sample was mounted into a polishing fixture by parafin wax. The sample face was polished with a series of silicon carbide polishing papers ranging from 15.3–2.5 μm grain size, ANSI grit: 600 (P1200), 800 (P2400), and 1200 (P4000) [24,25]. The polished sample was mounted under argon between two Biaxially-oriented polyethylene terephthalate (BoPET) sheets, known as Mylar®, in a

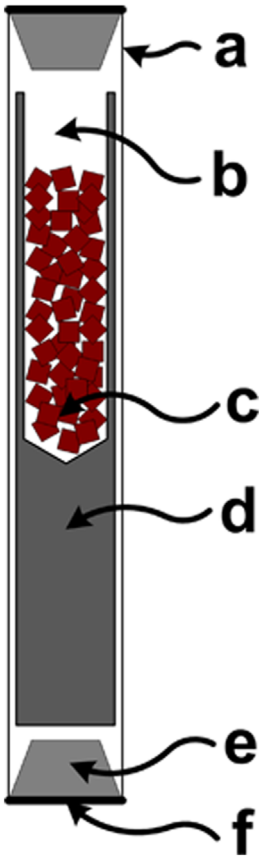

Fig. 2. Cross section of the loaded tantalum vessel. a–tantalum tube, b–argon gas, c–LiZnP material, d–pyrolytic graphite crucible, e–tantalum cap and f–air-tight arc weld.

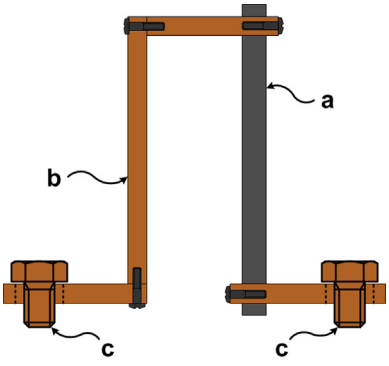

Fig. 3. Schematic of the oxygen-free *copper harness*. a–tantalum ampoule, b–oxygen-free copper and c–electrodes that connect to the low voltage power source.

custom sample holder designed to keep the sample air-tight, and then evaluated on a Bruker AXS Inc. D2 CRYSO energy-dispersive x-ray diffractometer. The measurements evaluated the crystal structure, orientation, lattice constant and *d* spacing. The sample was then mounted into an air-tight poly(methyl methacrylate) (PMMA) plastic sample holder with a beryllium dome with double sided tape as shown in Fig. 4. The particular sample was evaluated while under argon by a Bruker AXS Inc. high-resolution D8 DISCOVER x-ray diffractometer. The diffractometer was equipped with molybdenum optics with a four bounce monochromator (0.004° beam divergence), and a line beam 12.0 mm tall by

Fig. 4. Air-tight sample holder provided by Bruker AXS Inc. The sample holder consists of a PMMA base with double-sided sticky tape (left) and PMMA dome (right) that screws firmly to the o-ring seal on the base.

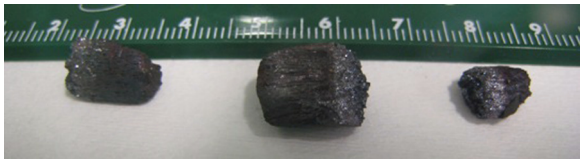

Fig. 5. LiZnP crystals grown by the high-temperature growth method (picture collected through the glove box window).

9.5 mm width (slit size). The sample was evaluated using phase identification scans, rocking curves and off axis measurements.

3. Results and disscussion

3.1. Bulk crystal growth

The bulk crystal growth process produced ingots of various size, the largest being $13.0 \times 9.0 \times 6.0\ mm^3$, as shown in Fig. 5. The ingot grown from purified material was 9.6 mm in diameter and 4.0 mm in length. A slice of the purified ingot is shown in Fig. 6. It was evident that the melting temperature reported by Kuriyama was not confirmed, nor observed in this study [6]. Numerous attempts to grow LiZnP by melt in crucible lined quartz ampoules always resulted in non-congruent melting up to temperatures of 1150 °C. Temperatures above 1150 °C in quartz resulted in the expansion of the soft quartz due to the high vapor pressure in the ampoule, and often resulted in ampoule rupture. Bulk crystal growth of LiZnP requires temperatures slightly above the threshold of conventional resistive coil furnaces that typically have a 1200 °C upper limit under continuous operation. Optical thermometer readings sampled through a quartz window of the crystal growth chamber, typically indicated a process/growth temperature between 1335–1355 °C (depending on the focus of the optical thermometer), which allowed for the congruent melt of LiZnP.

3.2. x-ray diffraction measurements

The polished LiZnP sample is shown in Fig. 7. The sample was sandwiched between sheets of Mylar® for protection against moisture and air. The $4.077 \times 3.518\ mm^2$ sample face was evaluated for crystal structure, lattice constant, *d* spacing, and orientation with a Bruker D2 CRYSO energy-dispersive x-ray diffractometer. The EDXRD method utilizes a Rhodium x-ray source that produces a polychromatic x-ray beam, a monocapillary optic to

Fig. 6. Slice from the LiZnP purified ingot (picture collected through the glove box window).

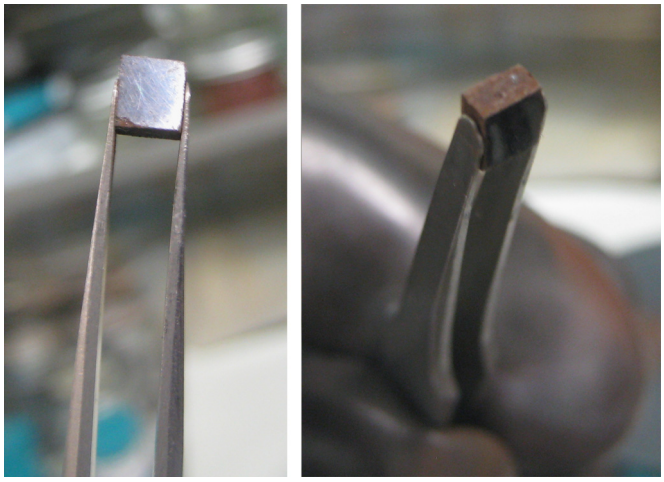

Fig. 7. A $4.077 \times 3.518 \times 2.020\ mm^3$ purified bulk grown LiZnP sample.

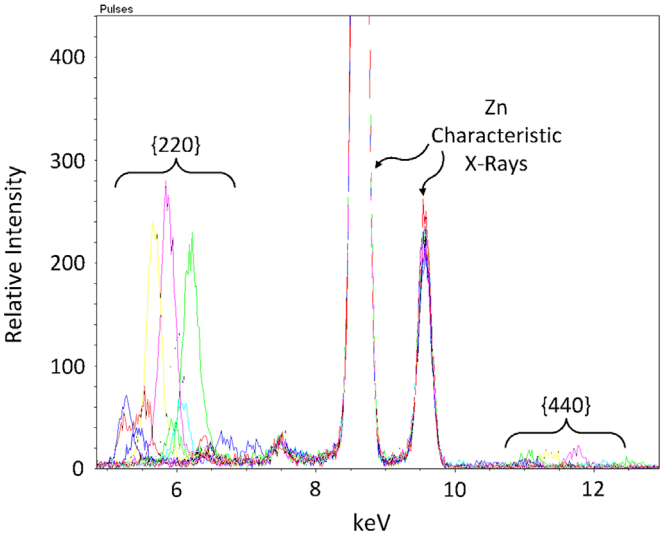

Fig. 8. The energy dispersive XRD spectrum collected on the polished LiZnP sample. Laue peaks from {220} and {440} LiZnP were observed.

collimate the x-ray beam to a spot, and an energy dispersive silicon drift detector. Energy plots from the diffracted beam are collected as the sample is rotated about the crystal surface normal (phi). Peaks in the diffracted energy plots correspond to Laue reflections from the crystal. The out of plane d spacing, degree of miscut and main orientation can be determined from these plots [26]. A collection of Laue peaks were observed for energy ranging between 5.0–6.5 keV, as shown in Fig. 8. The mere observation of these peaks proved that the sample was crystalline. In addition,

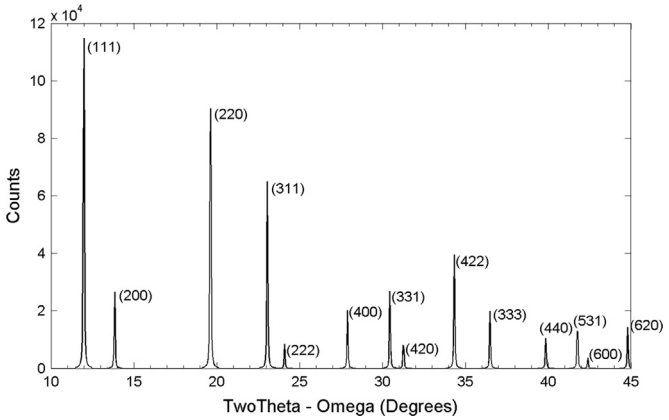

Fig. 9. The theoretical phase identification plot calculated with PowderCell 2.4 with a lattice constant of 5.885 Å.

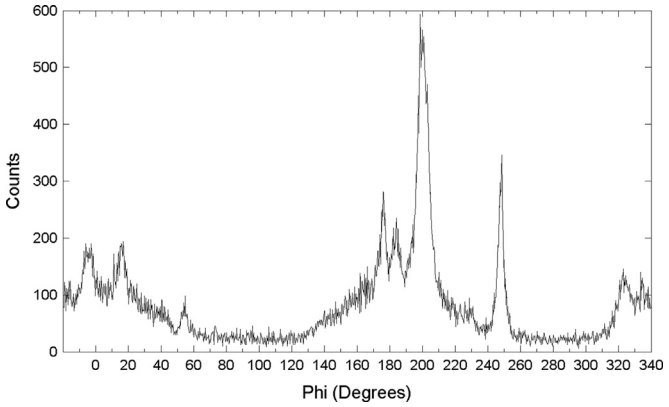

Fig. 10. A ϕ scan of the (220) main orientation. The array of peaks indicates presence multiple facets.

these peak locations were used to determine the main orientation, crystal structure, lattice constant and d spacing, by comparing to theoretical locations. A *guess* of the crystal structure, orientation and lattice constant was programed into the Bruker AXS Inc. software that calculated the theoretical peak positions based on the input parameters, and compared these locations to the experimental peak locations. The best fit to theoretical calculations was determined to be a cubic crystal structure with main orientation of (220), a lattice constant of 5.885 Å, and d spacing of 2.081 Å. The lattice constant was slightly higher than that of what was determined from the synthesized material [1].

The expected phase identification pattern was determined for LiZnP using PowderCell 2.4, shown in Fig. 9 [27]. The calculation was based on the lattice constant determined from the EDXRD lattice constant result, 5.885 Å, and molybdenum optics of a 0.71 Å wavelength. High-resolution phase identification scans were performed on the sample. Diffraction was observed at $2\theta = 19.4620^\circ$ and $\Omega = 10.7294^\circ$. Next, a ϕ scan (sample is rotated along the azimuthal direction) was performed. From Fig. 10, it is evident that multiple facets are present. Intensity was maximized by adjusting the ϕ angle on the most intense peak i.e. 199.94°, and phase identification scans were collected as shown in Fig. 11. The (220) orientation was clearly prominent at a 2θ of 19.46°, which confirms with the EDXRD result. In addition, the (440) orientation was observed at a 2θ of 39.48° and matches well with the theoretical position. The (440) orientation was also seen in the EDXRD scan where corresponding Laue peaks were observed between 10.75–12.5 keV as seen in Fig. 8. The crystalline ordering along the out of plane direction was examined by carrying out open detector rocking curves using a 4 bounce monochromator

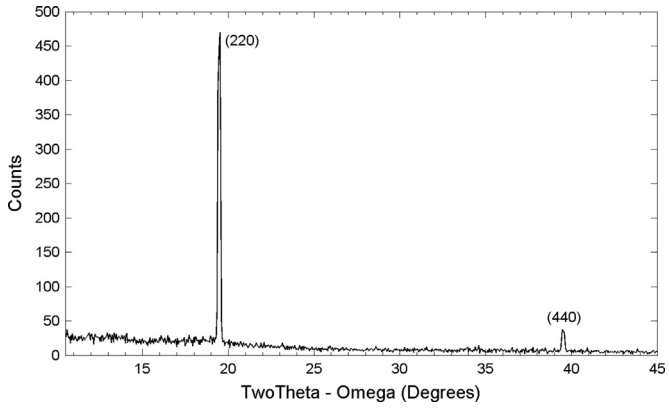

Fig. 11. Out-of-plane LiZnP phase identification scan.

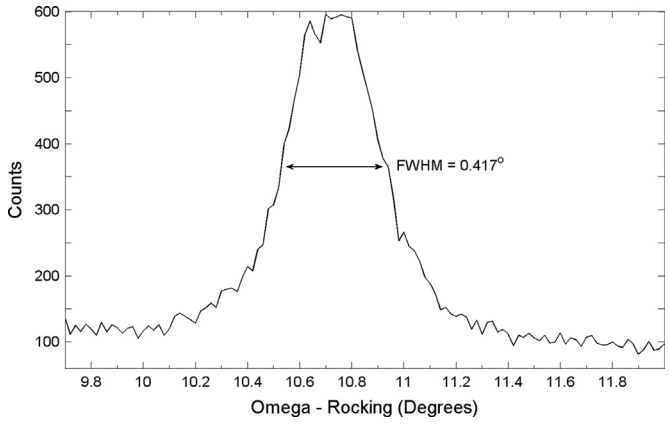

Fig. 12. Open detector (220) LiZnP rocking curve. A FWHM of 0.417° was determined.

Table 1
The angle between the (220) plane and the selected crystalline plane.

(hkl) plane	Angle
(422)	30°
(311)	31.48°
(222)	35.26°
(400)	45°

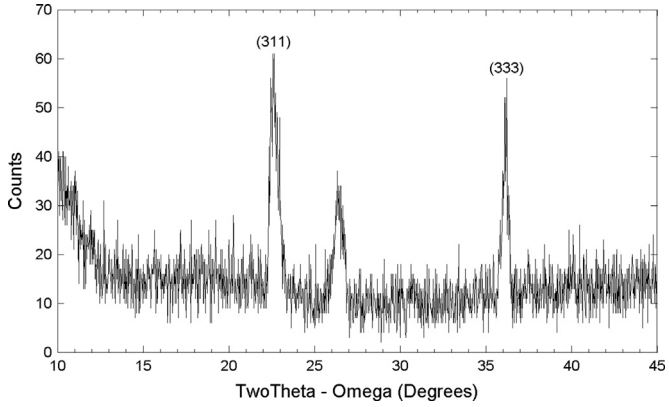

Fig. 13. A phase identification measurement at a ψ of 32.8560°. The (311) and (333) orientations were identified.

and an open detector. A (220) full width at half maximum (FWHM) of 0.417° was recorded as shown in Fig. 12. A rocking curve performed on a Single Crystal Silicon standard (from Bruker AXS) yielded a FWHM of

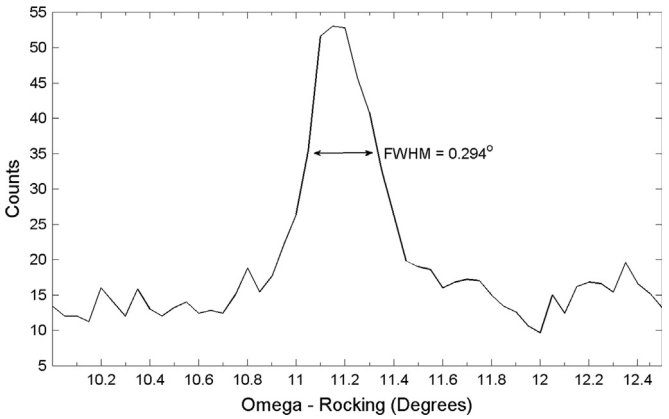

Fig. 14. Open detector (311) LiZnP rocking curve. A FWHM of 0.294° was observed.

0.004 degrees (14.4 arcsec) for the Si (111) reflection, which indicates that the rocking curve FWHM broadening of the LiZnP sample is primarily coming from the mosaicity of the sample.

The ψ axis (sample tilt) of the cradle, was utilized to explore the in-plane ordering of the sample. The angle between the (220) plane and other planes of interest are listed in Table 1. Diffraction was observed at a ψ of 32.8560°. A phase identification scan was collected which produced three prominent orientations, which is further indication that the sample is not a perfect single crystal as shown in Fig. 13. The peak located at 22.6° 2θ likely corresponds to the (311) orientation, which is theoretically located at 23.05° 2θ for LiZnP with a lattice constant of 5.885 Å. The peak located at 36.2° matches nicely to the theoretical position of the (333) LiZnP with a lattice constant of 5.885 Å. However, the peak located at 26.3° 2θ does not match well with the theoretical position for (222) LiZnP, with a lattice constant of 5.885 Å. These results indicate that grain boundaries exist in the evaluated area of the sample, and multiple domains could exist. In addition, these domains may have a shift in lattice constant from what was seen in the (220) main orientation. At the same angle of ψ (32.8560°), the 2θ axis was positioned at the (311) reflection and a rocking curve was collected, as shown in Fig. 14. The FWHM was determined to be 0.294°. The same order of magnitude FWHM was determined for the out-of-plane (220) and off axis (311) measurements, indicating a reasonable degree of crystallinity in the out-of plane and in-plane directions.

4. Conclusions

The largest known crystalline ingots of LiZnP were grown by a modified Bridgman high temperature method. LiZnP crystal growth was performed successfully in pyrolytic graphite crucible lined tantalum vessels. The melting temperature observed was experimentally determined to be between 1320–1370 °C. A LiZnP sample exhibited a (220) main orientation with a lattice constant of 5.885 Å as characterized by EDXRD and high-resolution XRD. A reasonable degree of crystallinity and ordering was observed for the out-of-plane and in-plane directions. Future work will include electrical characterization (resistivity, mobility-lifetime, trapping time), and neutron sensitivity measurements.

Acknowledgments

Work funded in part by the Advanced Materials Program DOE–NNSA, Grant DE-FG52-08NA28766.

References

[1] B.W. Montag, M.A. Reichenberger, K.R. Arpin, et al., Synthesis and characterization of LiZnP and LiZnAs semiconductor material, J. Cryst. Growth 412 (2015) 103–108.

[2] B.W. Montag, M.A. Reichenberger, P.B. Ugorowski, et al., Static sublimation purification process and characterization of LiZnP semiconductor material, J. Cryst. Growth in press.

[3] R. Juza, K. Langer, K. Von Benda, Ternary nitrides, phosphides, and arsenides of Lithium, Angew. Chem. Int. Edit. Engl. 7 (5) (1968) 360–370.

[4] H. Nowotny, K. Bachmayer, Die Verbindungen LiMgP, LiZnP und LiZnAs, Monatshefte für Chem. und verwandte Teile anderer Wiss. 81 (4) (1950) 488–496.

[5] D. Kieven, A. Grimm, A. Beleanu, et al., Preparation and properties of radio-frequency-sputtered half-Heusler films for use in solar cells, Thin Solid Films 519 (6) (2011) 1866–1871.

[6] K. Kuriyama, T. Katoh, N. Mineo, Crystal growth and characterization of the filled tetrahedral semiconductor lithium zinc phosphide (LiZnP), J. Cryst. Growth 108 (1–2) (1991) 37–40.

[7] K. Kuriyama, T. Katoh, Optical band gap of the filled tetrahedral semiconductor lithium zinc phosphide (LiZnP), Phys. Rev. B: Condens. Matter 37 (12) (1988) 7140–7142.

[8] R. Bacewicz, T.F. Ciszek, Preparation and characterization of some $A^{I}B^{II}C^{V}$ type semiconductors, Appl. Phys. Lett. 52 (14) (1988) 1150–1151.

[9] Z.W. Bell, K.R. Pohl, L. Van Den Berg, Neutron detection with mercuric iodide, IEEE Trans. Nucl. Sci. 51 (3) (2004) 1163–1165.

[10] A.G. Vradii, M.I. Krapivin, L.V. Maslova, et al., Possibilities of recording thermal neutrons with cadmium telluride detectors, Sov. At. Energy 42 (1) (1977) 64–66.

[11] A.G. Beyerle, K.L. Hull, Neutron detection with mercuric iodide detectors, Nucl. Instrum. Methods A 256 (2) (1987) 377–380.

[12] D.S. McGregor, J.T. Lindsay, R.W. Olsen, Thermal neutron detection with $cadmium_{1-x}$ $zinc_x$ telluride semiconductor detectors, Nucl. Instrum. Methods A 381 (2) (1996) 498–501.

[13] Y. Kumashiro, K. Kudo, K. Matsumoto, et al., Thermal neutron irradiation experiments on ^{10}BP single-crystal wafers, J. Less Common Met. 143 (1–2) (1988) 71–75.

[14] W.C. McGinnis, Film Implementation of a Neutron Detector (FIND): proof of concept device, Technical Report 1921, 2003.

[15] J.C. Lund, F. Olschner, F. Ahmed, et al., Boron phosphide on Silicon for radiation detectors, MRS Online Proc. Libr. 162 (1989) 601–604.

[16] F.P. Doty, Boron nitride solid state detector, US-6, 504, April 27, 2004, US-6,727,504, April 27, 2004.

[17] A.N. Caruso, P.A. Dowben, S. Balkir, et al., The all boron carbide diode neutron detector: comparison with theory, Mater. Sci.and Eng. B 135 (2) (2006) 129–133.

[18] B.W. Robertson, S. Adenwalla, A. Harken, et al., A class of boron-rich solid-state neutron detectors, Appl. Phys. Lett. 80 (19) (2002) 3644–3646.

[19] P. Groot, J.H.F. Grondel, P.J. v.d.Put, Chemical vapour deposition of boron phosphides using bromide etchants, Solid State Ion. 16 (1985) 95–98.

[20] A.N. Caruso, R.B. Billa, S. Balaz, et al., The heteroisomeric diode, J. Phys. Condens. Matter 16 (2004) L139–L146.

[21] D.S. McGregor, M.D. Hammig, Y.H. Yang, et al., Design considerations for thin film coated semiconductor thermal neutron detectors—I: basics regarding alpha particle emitting neutron reactive films, Nucl. Instrum. Methods A 500 (1–3) (2003) 272–308.

[22] R. Bacewicz, T.F. Ciszek, Crystal growth and characterization of some novel $A^{I}B^{II}C^{V}$ semiconductors, Acta Phys. Pol. A A77 (2–3) (1990) 379–381.

[23] K. Kuriyama, T. Katoh, S. Tsuji, Preparation and characterization of the filled tetrahedral semiconductor lithium zinc phosphide film on quartz, J. Appl. Phys. 66 (8) (1989) 3945–3947.

[24] K. Geels, Metallographic and Materialographic Specimen Preparation, Light Microscopy, Image Analysis and Hardness Testing, ASTM International, West Conshohocken, PA, 2007.

[25] Pace Technologies, Abrasive Grinding Paper, ⟨http://www.metallographic.com/Brochures/SiCpaper.pdf⟩.

[26] Bruker AXS Inc, brochure_D2_CRYSO.pdf, ⟨http://bruker.poznan.pl/images/stories/AXS/brochure_D2_CRYSO.pdf⟩, 2009.

[27] W. Kraus, G. Nolze, POWDER CELL – a program for the representation and manipulation of crystal structures and calculation of the resulting x-ray powder patterns, J. Appl. Cryst. 29 (3) (1996) 301–303.